



Published in final edited form as:

*Oncogene*. 2021 April ; 40(16): 2884–2897. doi:10.1038/s41388-021-01728-2.

## Isolating and targeting the real-time plasticity and malignant properties of epithelial-mesenchymal transition in cancer

Hector Esquer<sup>1,†</sup>, Qiong Zhou<sup>1,†</sup>, Travis Nemkov<sup>2</sup>, Adedoyin D. Abraham<sup>1</sup>, Sébastien Rinaldetti<sup>1</sup>, Yu-Chi Chen<sup>4</sup>, Xiaohu Zhang<sup>4</sup>, Michael V. Orman<sup>1</sup>, Angelo D'Alessandro<sup>2,5</sup>, Marc Ferrer<sup>4</sup>, Wells A. Messersmith<sup>3,5</sup>, Daniel V. LaBarbera<sup>1,5,\*</sup>

<sup>1</sup>The Skaggs School of Pharmacy and Pharmaceutical Sciences, Department of Pharmaceutical Sciences; The School of Medicine,

<sup>2</sup>Department of Biochemistry and Molecular Genetics, National Center for Advancing Translational Sciences (NCATS), National Institutes of Health (NIH), Rockville, Maryland.

<sup>3</sup>the Division of Medical Oncology, National Center for Advancing Translational Sciences (NCATS), National Institutes of Health (NIH), Rockville, Maryland.

<sup>4</sup>Early Translation Branch, National Center for Advancing Translational Sciences (NCATS), National Institutes of Health (NIH), Rockville, Maryland.

<sup>5</sup>The University of Colorado Cancer Center (UCCC); The University of Colorado Anschutz Medical Campus (CU AMC), Aurora CO.

### Abstract

Epithelial-mesenchymal transition (EMT) is a driving force in promoting malignant cancer, including initiation, growth, and metastasis. EMT is a dynamic process that can undergo a mesenchymal-epithelial transition (MET) and partial transitions between both phenotypes, termed epithelial-mesenchymal plasticity (EMP). In cancer, the acquisition of EMP results in a spectrum of phenotypes, promoting tumor cell heterogeneity and resistance to standard of care therapy. Here we describe a real-time fluorescent dual-reporter for vimentin and E-cadherin, biomarkers of the mesenchymal and epithelial cell phenotypes, respectively. Stable dual-reporter cell lines generated from colorectal (SW620), lung (A549), and breast (MDA-MB-231) cancer demonstrate a spectrum of EMT cell phenotypes. We used the dual-reporter to isolate the quasi epithelial, epithelial/mesenchymal, and mesenchymal phenotypes. Although EMT is a dynamic process, these isolated quasi-EMT-phenotypes remain stable to spontaneous EMP in the absence of stimuli and during prolonged cell culture. However, the quasi-EMT phenotypes can readily be induced to undergo EMT or MET with growth factors or small molecules. Moreover, isolated EMT phenotypes display different tumorigenic properties and are morphologically and metabolically distinct. 3D high-content screening of ~23,000 compounds using dual-reporter mesenchymal

Users may view, print, copy, and download text and data-mine the content in such documents, for the purposes of academic research, subject always to the full Conditions of use:[http://www.nature.com/authors/editorial\\_policies/license.html#terms](http://www.nature.com/authors/editorial_policies/license.html#terms)

\* **Corresponding Author Information:** D.V.L.: [daniel.labarbera@cuanschutz.edu](mailto:daniel.labarbera@cuanschutz.edu), 12850 E. Montview Boulevard, Room V20-2101, Aurora CO, 80045.

† Contributed equally to this work as co-first authors.

Competing Interests

The authors declare no competing interests.

SW620 tumor organoids identified small molecule probes that modulate EMT, and a subset of probes that effectively induced MET. The tools, probes, and models described herein provide a coherent mechanistic understanding of mesenchymal cell plasticity. Future applications utilizing this technology and probes are expected to advance our understanding of EMT and studies aimed at therapeutic strategies targeting EMT.

## Introduction

Malignant cancer develops from the contribution of multiple factors known as the hallmarks of cancer, which also promote tumor cell heterogeneity, multi-drug resistance (MDR), and evasion of the immune response<sup>1</sup>. In particular, the epithelial-mesenchymal transition (EMT) program is a hallmark that transforms tumor cells into a spectrum of EMT phenotypes that have diverse tumorigenic and metastatic properties<sup>1-4</sup>. This spectrum includes stable epithelial (xE) and mesenchymal (xM) states and quasi-states, including the epithelial (E), hybrid (E/M), and mesenchymal (M) cell populations<sup>5</sup>. Notably, the stable xE and xM states are less malignant compared to the quasi-states, which are known to be transient and reversible between EMT and mesenchymal-epithelial transition (MET)<sup>4, 5</sup>. The ability of carcinomas to readily cross between both states has been termed epithelial-mesenchymal plasticity (EMP)<sup>6</sup>, which is implicated as a driving force promoting tumor growth, metastasis, and MDR. EMP involves an elaborate network of transcription factors and regulatory pathways that complicate its mechanistic study, limiting the development of targeted therapies against EMT<sup>2</sup>.

EMT phenotypes are characterized and distinguished using biomarkers, notably, E-cadherin (epithelial) and vimentin (mesenchymal)<sup>7</sup>. Loss of E-cadherin and gain of vimentin are also clinical biomarkers of poor prognosis for many types of cancer<sup>8-14</sup>. Therefore, to address the challenges associated with EMP, we have developed an EMT dual fluorescent reporter for the promoter regions of E-cadherin and vimentin (dual-reporter). When the dual-reporter is transduced into cancer cells, it functions as an effective tool to measure EMP in real time while simultaneously tracking the spectrum of EMT cellular phenotypes. Furthermore, EMT phenotypes can be isolated by fluorescence activated cell sorting (FACS) based on dual-reporter fluorescence. Herein, we demonstrate the ability to isolate and characterize quasi-EMT phenotypes that are morphologically and metabolically distinct<sup>15</sup>. To the best of our knowledge, our studies are the first to demonstrate these metabolic differences in isolated EMT cell phenotypes, providing a more accurate picture of EMT driven heterogeneity without the addition of external stimuli or genetic manipulation.

The results of this study led to the hypothesis that depletion of the M-phenotype may decrease metastasis and sensitize primary tumors and metastatic lesions to clinical therapies, and potentially reduce the probability of patient mortality. Prompted by our hypothesis, we developed a dual-reporter SW620 M-phenotype colorectal cancer (CRC) tumor organoid model that is validated for 3D high-content screening (HCS) of tens of thousands of compounds to identify small molecule probes that modulate or reverse EMT. Through this HCS model, we discovered and validated lead EMT probes that induce MET and decrease malignant properties in isolated quasi-mesenchymal tumor organoids, which shed light on

the mechanisms controlling EMP in CRC. We anticipate that these tools, probes, and models can be adapted to a variety of cancers, therefore, facilitating the study of mechanisms controlling EMT-driven tumor progression and metastasis, and the discovery of new drug therapies.

## Results

### The isolation of distinct EMT phenotypes in colorectal, lung, and breast cancer.

Vimentin and E-cadherin are established biomarkers of EMT<sup>16, 17</sup>. We designed a lentiviral plasmid that reports on the promoter activity of vimentin (VimPro-GFP) and E-cadherin (EcadPro-RFP) with dual expression of two fluorescent proteins (Fig. 1a). We transduced three carcinoma lines, SW620 (CRC), A549 (lung), and MDA-MB-231 (breast), to identify and assess EMT phenotypes using the dual-reporter. Image-based high-content analysis (HCA) revealed that each cancer type possessed three populations with high dual-reporter activity, RFP+, RFP+/GFP+, GFP+, and one population that had low dual-reporter activity (<100 RFU) that we define as RFP-/GFP- (Fig. 1b-d). Because the RFP-/GFP- represented approximately half of the cell population in each cancer type, we evaluated the success of our transduction using PCR analysis (Fig. S1a-c). The PCR results demonstrate that the RFP-/GFP- population was successfully transduced with the dual-reporter. Intrigued by the low reporter activity, we next evaluated the difference between low and high dual-reporter activity populations using Integrin- $\beta$ 4 (aka CD104) positive and CD44 high expression (CD104+/CD44+), which is reported as an effective marker in a variety of cancer types that distinguishes the more malignant quasi-EMT states from the stable-EMT states<sup>5, 18</sup>. The dual-reporter transduced cell lines were stained with antibodies for CD104 and CD44 and analyzed by flow cytometry (Fig. S2). The results demonstrate that the high dual-reporter activity cell populations (RFP+, RFP+/GFP+, and GFP+) are higher in CD104+/CD44+ expression compared to the dual-reporter low activity (RFP-/GFP-) cell population. This result indicates that the RFP-/GFP- cell population likely harbors the stable EMT-populations, described by Kröger *et al.* to be less tumorigenic compared to the quasi-EMT population<sup>5</sup>. Importantly, higher CD104+/CD44+ expression definitively marks EMT positive cells with increased mesenchymal character and cancer stem cell (CSC) stemness<sup>5, 18</sup>. Therefore, we prioritized the CD104+/CD44+ quasi-EMT dual-reporter active populations moving forward. Next, we enriched and isolated the three distinct dual-reporter active quasi-EMT cell populations based on dual-reporter fluorescence by FACS, which we define as E (RFP+), E/M (RFP+/GFP+), and M (GFP+) (Fig. 1e-g). The protein expression of the epithelial and mesenchymal biomarkers is consistent for the E, E/M, and M phenotypes, respectively (Fig. 1h-j). Notably, the expression of these biomarkers is also consistent with EMT populations displaying higher expression of CD104+/CD44+<sup>5</sup>.

### Isolated quasi-M-phenotypes have increased tumorigenic potential.

In Fig. 1 and Fig. S2, we demonstrate that the dual-reporter activity high cell population has increased mesenchymal traits. To further characterize the mesenchymal character of isolated EMT phenotypes we examined the expression ratio of CD44 and CD24 surface markers, which are widely used markers to distinguish epithelial from mesenchymal carcinoma

cells<sup>18</sup>. In addition, high CD44 surface marker expression is a marker for increased tumor initiating cell properties (also referred to as CSCs) such as stemness and invasiveness<sup>19–22</sup>. As determined by flow cytometry, the mean CD44/CD24 fluorescence ratio was highest in MDA-MB-231 cells, followed by A549 and SW620 cells (Fig. 2a). Interestingly, the levels of CD44<sup>high</sup>/CD24<sup>low</sup> expression correlates with the magnitude of the difference of the number of M- to E-phenotype cells, as sorted by the dual-reporter expression. MDA-MB-231 cells have the highest CD44<sup>high</sup>/CD24<sup>low</sup> expression and both the highest number of M-positive cells and the largest difference between percent of populations of E- and M-phenotypes (Fig. 2b and Fig. S3). We assessed the stemness potential of the cell lines by their ability to form clonogenic colonies<sup>23, 24</sup>. The clonogenic assay further supported that the vimentin high M-phenotypes have a significant increase in stemness compared to the E- and E/M-phenotypes (Fig. 2c and Fig. S4). Notably, CD104<sup>+</sup>/CD44<sup>+</sup> and CD44<sup>high</sup>/CD24<sup>low</sup> were effective markers indicating more malignant quasi-EMT states and increased mesenchymal stemness character, respectively (Fig. 2 and Fig. S2). The M-phenotype also displays a higher invasive potential compared to the E-phenotype (Fig. 2d). These results demonstrate that the dual-reporter is an effective tool to enrich for quasi-EMT phenotypes that vary in their mesenchymal character and tumorigenic potential.

### **Isolated EMT phenotypes are stable to spontaneous EMP but readily undergo induced EMP.**

Recently, CD104<sup>+</sup>/CD44<sup>+</sup> expression was used to mark quasi-EMT cells that proved to be stable to spontaneous EMT and MET, yet these cells could be induced through EMT and MET by genetic manipulation<sup>5</sup>. Likewise, dual-reporter quasi-EMT cell populations also displayed higher expression of CD104<sup>+</sup>/CD44<sup>+</sup>. To determine the stability of isolated phenotypes in long-term sub-culture, we performed HCA of the fluorescent phenotypes and of their morphology, through supervised machine learning (Fig. S5 and Tables S1 and S2). The dual-reporter fluorescent activity of each phenotype showed that the isolated EMT phenotypes are stable under long-term culture in the absence of external stimuli measured by dual-reporter activity (Fig. S5a,d,g). Supervised machine learning quantitated the morphologies of the different phenotypes revealing that the E- and M-phenotypes are dominated by a cobble-shaped or spindle-shaped morphology, respectively (Fig. S5c,f,i). These morphologies align with the common morphological distinctions between these two phenotypes<sup>25</sup>. Interestingly, the E/M morphology appears to be a close representation of the parental cell line's relative expression of E-cadherin and vimentin (Fig. S5c,f,i). Furthermore, culturing cells as monolayers (2D) or tumor organoids (3D) with extracellular matrix (ECM) does not alter dual-reporter activity (Fig. S5b,e,h). Finally, the supervised machine learning results were analyzed by principal component analysis (PCA) using 400 different morphological parameters to distinguish between the different morphologies of the E, E/M, and M phenotypes (Fig. S5j–l). The results demonstrate that the dual-reporter can isolate distinct EMT phenotypes that remain stable to spontaneous EMP in long-term cell culture.

To determine if dual-reporter quasi-EMT cell populations can be induced through EMP, we treated unsorted dual-reporter transduced PMC42LA cells with epidermal growth factor (EGF) (Fig. S6)<sup>26, 27</sup>. EGF induces EMT, based on dual-reporter activity and protein

expression, decreasing the E- and E/M-phenotypes while increasing the M-phenotype compared to control. We previously described the development and characterization of TOP2A ATP-competitive inhibitors and their ability to prevent Wnt/TCF/LEF-transcription (denoted as TCF-transcription) thereby inducing MET and reversing the tumorigenic potential in CRC<sup>28, 29</sup>. Using the TOP2A inhibitor compound **7**, we tested the ability to induce MET in SW620 M-phenotype tumor organoids measuring dual-reporter activity. Compound **7** effectively induced MET compared to DMSO control measured by 3D HCA time-lapse imaging over 3-days (Video S1). In conclusion, the dual-reporter is an effective tool to quantify spontaneous or induced EMP in real-time.

### Isolated EMT populations are metabolically distinct.

While the dual-reporter proved to be useful in isolating distinct E, E/M, and M phenotypes we sought to further characterize and distinguish these differences using a MS-based metabolomics approach to determine metabolic characteristics (metabotypes) of isolated quasi-EMT phenotypes (Supplementary Metabolomics Table). In line with the distinct morphological characteristics (Fig. S5), unsupervised PCA of metabolite abundance similarly determined unique, independent clustering patterns for isolated E, E/M, and M dual-reporter tumor organoids derived from SW620, A549, and MDA-MB-231 cell lines (Fig. 3a–c). These observations were further emphasized by hierarchical clustering analysis, which also distinguished these EMT phenotypes based on the relative abundance of metabolites (Fig. 3d–f). Interestingly, while E- and M-phenotypes could be similarly distinguished by principal component 1 in all cell lines, which explained between 32.5% and 48.8% of the metabolic variability, the relative clustering of the hybrid E/M population was cell line-dependent. In line with recent observations of unique metabotypes across various cancer cell lines<sup>30</sup>, the metabolites that contributed to clustering patterns observed in our study were also cell-line specific (Fig. 3, Fig S7, and Supplementary Metabolomics Table). For example, while lactate was highest in the M-phenotype of SW620 cells, it was the E-phenotype in A549 cells, and E/M-phenotype in MDA-MB-231 cells that appeared to have an upregulation of glycolysis. In addition, the MDA-MB-231 M-phenotype had significantly higher TCA cycle metabolites relative to the E-phenotype while this relationship was only partially recapitulated in the SW620 and A549 cells.

### Small molecule induced MET in the M-phenotype measured by metabolomics.

To determine the metabolic underpinnings of these observations, we treated SW620 tumor organoids comprised of M-phenotype cells with Compound **7** (M+**7**) and compared the subsequent metabotype with that of the E-phenotype tumor organoid using metabolomics that had been previously collected. To control for batch variability in the mass spectrometer as these datasets were collected separately, we normalized metabolite levels in each dataset (SW620 M vs E; SW620 M vs M+**7**) to the median M value in the respective dataset, as these tumor organoids were cultured for both sets of experiments. We then employed PCA to identify metabolites in M cells that return to the relative levels in E-phenotype cells when treated with Compound **7** (Fig 4a). While Component 1 primarily described cumulative differences between E and M+**7** cells and accounted for 31.1% of the variability, Component 2 accounted for 24.4% of the variability and predominantly described shared differences between E and M+**7** organoids compared to their M-phenotype counterparts,

while Component 3 (11% of the variability) related to intragroup technical variability. PCA of metabolomics data demonstrated that E- and M+7 tumor organoids clustered independently of M-phenotype tumor organoids along the Component 2 axis and were statistically indistinguishable from one another. Analysis of the top 25 metabolites that influenced this clustering pattern highlighted multiple metabolites that are centrally involved in energy homeostasis, including nucleotide levels, glycolysis, and the TCA cycle (Fig. 4b). We also observed that M-phenotype cells have enhanced glycolysis (lower glucose and higher lactate), as well as altered PPP utilization (lower oxidative phase 6-phosphogluconate and higher non-oxidative phase erythrose-4-phosphate) (Fig. 4c). Significant higher levels of TCA cycle intermediates  $\alpha$ -ketoglutarate ( $\alpha$ -KG) and fumarate, and overall higher energy status (ATP/AMP ratio) indicate alterations in substrate preference between the E- and M-phenotype cell populations (Fig. 4c). Mesenchymal cells also possess higher levels of acylcarnitines, including decanoylcarnitine (AC C10), dodecanoylcarnitine (AC C12:1), and tetradecanoylcarnitine (AC C14) that are essential for fatty acid oxidation (Fig. 4b)<sup>31</sup>. Because fatty acid oxidation yields a higher overall amount of ATP compared to glucose, a specific preference for fatty acid oxidation in M-phenotype cells would be consistent with the observed higher overall levels of ATP in the absence of isotope tracing analysis. In view of observations that the plasticity of CSCs may depend on the ability to import fatty acids for oxidation<sup>32, 33</sup>, these data support increased stemness observed to correlate with vimentin expression in the M-phenotypes (Fig. 2c). Strikingly, treatment with Compound 7 appears to reverse the levels of each of these metabolites back towards or below relative levels observed in the E-phenotype tumor organoids (Fig. 4b,d). These observations highlight that E- and M-phenotype tumor cell populations are metabolically distinct but can be manipulated through pharmacological intervention at the level of transcriptional changes that drive EMT and EMP.

### 3D high-content screening targeting EMP in quasi-M-phenotype CRC tumor organoids.

The quasi-M-phenotype is known to be more malignant compared to other EMT phenotypes<sup>4</sup>, and our results with the different isolated EMT phenotypes are consistent with this scientific premise. In addition, Kröger *et al.*<sup>5</sup> recently reported the isolation of a quasi-EMT phenotype (which they termed E/M) with increased mesenchymal character (marked by increased CD104+/CD44+ expression) and tumorigenic properties in breast cancer cells. This E/M phenotype also displayed significantly higher TCF-transcriptional activity, regulated through the canonical Wnt pathway. Similarly, we and others have reported that TCF-transcription functions as a master regulator of EMT in CRC<sup>29, 34</sup>. To further investigate the role of TCF-transcription in promoting the quasi-M-phenotype in CRC we transiently transfected unsorted and sorted dual-reporter SW620 cells with the luminescent TCF-transcriptional reporter (TOPflash)<sup>28, 29</sup>. Comparatively, the isolated M-phenotype displayed 3-to-4-fold higher TCF-activity than the isolated E, E/M, and RFP-/GFP- phenotypes (Fig. S8). This result is consistent with the enhanced stemness and invasive potential observed with the M-phenotype (Fig. 2c,d), further validating the M-phenotype as having increased tumorigenic potential. Thus, we used FACS-sorted SW620 M-phenotype cells to conduct HCS with small molecules to discover probes regulating EMP in CRC with the goal of identifying compounds that reverse the M-phenotype to the more benign E-phenotype<sup>35</sup>.

Sorted M-phenotype SW620 cells were used to generate a single tumor organoid per well in the presence of ECM (Fig. S9 and Video S1). The dual-reporter activity was monitored over 3-days, including a negative control (0.5% DMSO, vehicle) and a positive control (compound **7** at 10  $\mu$ M) (Fig. S9)<sup>28, 36, 37</sup>. We conducted two separate pilot screens at CU AMC (Spectrum Library) and NCATS (Epigenetics library) (Fig. S10 and Table S3), which identified numerous hits that modulate EMT. However, only 9 hits (1 from Spectrum and 8 from Epigenetics) induce MET. Next, we conducted 3D HCS using the biological interrogation cassette (BIC) consisting of 20,799 compounds, obtained from Eli Lilly and Company's Open Innovation Drug Discovery (OIDD) program (Fig. S11 and Table S3). There were significantly more hits that modulate EMT (667 upregulate E-cadPro-RFP, while 902 downregulate VimPro-GFP) with a small subset of compounds that induce MET (27 hits). We prioritized probes that induce MET to more effectively target EMP. Combined, HCS yielded 36 hits that induce MET. Dose response studies validated 10 probes that induce MET in a dose dependent manner (Fig. 5a,b and Fig. S12). Finally, validated hits were prioritized as lead probes based on their ability to inhibit stemness (clonogenicity) and invasive potential (Fig. 5c,d and Fig. S12). These compounds included two Protein Kinase C (PKC) inhibitors (RO-31-8220 and RO-32-0432), one Aurora Kinase A/B/C (AURK) inhibitor (SNS-314), a Proviral Integration site for Moloney murine leukemia virus-1-Kinase (Pim) 1/2/3 inhibitor (CX-6258), a lysine methyltransferase / Cyclin-dependent Kinase 4 (KMT5A / CDK4) inhibitor (Ryuvidine), a Jumonji histone demethylase (JMJD2) inhibitor (ML324), and a Macrophage Migration inhibitory Factor / Vesicular Glutamate Transporter (MIF / VGLUT) inhibitor (Chicago Sky Blue, or CSB). In addition, three probes with no known molecular targets were validated from the BIC library, including W112130-B17, W111768-M14, and W112152-C05.

## Discussion

Herein, we present a unique dual-reporter of EMT as a powerful biological tool that allows for the isolation, interrogation, and real-time tracking of EMP and of distinct EMT phenotypes in well-established cancer cell lines. The results of this work demonstrate the inherent heterogeneity in cancer cells with respect to EMT states<sup>4</sup>, which can be exploited to study shifts in these populations driven by EMP. After sorting, EMT biomarker protein expression is maintained and correlates with promoter activity, demonstrating that isolated EMT phenotypes are stable to spontaneous EMP. Furthermore, the results illustrate unequivocal differences morphologically and metabolically between EMT phenotypes (Fig. 3 and Fig. S5). For example, by isolating subpopulations of MDA-MB-231 cells based on dual-reporter expression, we found that the E/M- and M-phenotypes had increased levels of lactate in MDA-MB-231 and SW620 cells, respectively, compared to the E-phenotype (Fig. S7). Notably, other groups have shown lactate as a marker that distinguishes metabolic states and as an oncometabolite that increases stemness<sup>38, 39-44</sup>.

Our results suggest that vimentin drives the stemness and invasive potential (Fig. 2). Thus, we pursued pharmacological reversion of the M-phenotype to its less stem-like and invasive E-phenotype. Indeed, treatment of CRC M-phenotype tumor organoids with compound **7** induces MET based on real-time dual-reporter activity and by metabolomics (Fig. 4 and Video S1). We validated this CRC tumor organoid model for 3D HCS of ~23,000

compounds. This screen identified hundreds of probes that modulate EMT but only a subset that induce MET, which were used to generate a coherent mechanistic understanding of mesenchymal cell EMP (Fig. 6). In particular, our metabolomics studies found that L-glutamate,  $\alpha$ -KG, and fumarate are significantly downregulated in the E-phenotype compared to the M-phenotype, and these metabolites fuel the TCA cycle. Intriguingly, these metabolites are linked to EMT probes via  $\alpha$ -KG, including CSB (VGLUT) and ML324 (JMJD2) (Fig. 5). CSB is an inhibitor of L-glutamate transport and loss of glutamate can alter the production of  $\alpha$ -KG. Moreover, these metabolites are utilized in many cellular processes as substrates for enzymatic activity, notably, the hypoxia response<sup>45</sup>. HIF-1 $\alpha$  is regulated in the cytoplasm via  $\alpha$ -KG dependent prolylhydroxylase (PHD) mediated proteasomal degradation. However, fumarate is a direct inhibitor of PHD leading to HIF-1 $\alpha$  nuclear translocation inducing the hypoxia response, including c-Myc upregulation<sup>45</sup>. Although hypoxia decreases the TCA cycle flow, c-Myc activates genes that replenish the TCA cycle via glutamine mitochondrial import, which is converted to  $\alpha$ -KG<sup>46</sup>. Additionally, the hypoxic response upregulates the PPP<sup>45</sup> and we observe this with increased erythrose-4-phosphate in the SW620 M-phenotype (Fig. 4).  $\alpha$ -KG is also linked to epigenetic events as a substrate used by JMJD histone demethylases. JMJD activates the EMT transcription factor Snail-1, which is an epigenetic negative regulator of E-cadherin<sup>47</sup>. Likewise, the lysine methyltransferase, KMT5A, is an epigenetic regulator of Wnt target genes, including cadherin switching<sup>47</sup>. Our results are consistent with this complex relationship between the TCA cycle, PPP, hypoxia, and epigenetic events that convey increased tumorigenic properties to the M-phenotype in CRC.

TCF-transcription is a master regulator of EMT, notably, ZEB1, Slug, N-cadherin, and c-Myc<sup>29, 34, 48</sup>. Moreover, the isolated SW620 M-phenotype displayed the highest TCF-activity compared to other EMT populations (Fig. S8). Indeed, treatment with **7**, induces MET, by downregulating TCF-transcription promoting antitumor activity (Fig. 4, Fig. S9, and Video S1)<sup>28, 29</sup>. Furthermore, crosstalk between the Wnt and Ras pathways is further implicated in regulating EMT as shown by lead probes RO318220 (PKC)<sup>49</sup> and SNS314 (AURK)<sup>50</sup> that induce MET. Therefore, both the Wnt and Ras pathways interact to promote EMT, and tumor progression in CRC<sup>51</sup>. Moreover, the SW620 M-phenotype has increased fatty acids, and fatty acid oxidation is known to activate the Ras MAPK pathway through MEK<sup>52</sup> (Fig. 6). Yet another connection with mesenchymal cell energetics, we identified that inhibition of Pim 1/2/3 by CX6258 reverses EMT. Pim kinases have been shown to regulate energy by increasing c-Myc and PGC-1 $\alpha$ , promoting glycolysis and downregulating AMPK (Fig. 6)<sup>53</sup>. Our results are consistent with this mechanism of Pim mediated energetics regulating EMT, demonstrating that the M-phenotype has higher ATP/AMP ratios compared to the E-phenotype (Fig. 4). Finally, in addition to being an inhibitor of VGLUT (aka SLC17A7), CSB is also a potent nM inhibitor of MIF<sup>54</sup>, which stimulates  $\beta$ -catenin nuclear translocation and TCF-transcription<sup>55</sup>. Since VGLUT has been primarily studied in the nervous system<sup>56</sup>, we assessed VGLUT expression in CRC using the cBioPortal (TCGA, Firehose Legacy) database. We found that its expression is low but has a significant positive correlation with vimentin, TCF4, and Snail-1 (Fig. S13). Thus, we postulate that the predominant on-target reversal of EMT is through CSB inhibition of MIF.

In conclusion, this report highlights novel tools and approaches to identify, isolate, and characterize EMT cell populations and their plasticity. These tools were used to validate a tumor organoid model of EMP in CRC for 3D HCS, which identified hundreds of EMT probes, including lead probes that induce MET. In addition, the information from metabolomics and lead probes were used to generate a coherent relationship of pathways regulating CRC quasi-M-phenotype plasticity (Fig. 6). We anticipate that these tools and probes will be employed for both *in vitro* and *in vivo* studies of EMT-driven tumorigenesis that will facilitate novel strategies to treat cancer.

## Methods

### Metabolomics.

Tumor organoids were prepared as previously described at 20,000 cells/well. The tumor organoids were incubated for 72h then treated with DMSO or **7** for an additional 72h. Afterwards, eight tumor organoids per condition were collected into 1.5 mL microcentrifuge tubes. Tumor organoids and medium were separated by centrifugation. Medium was stored in  $-80^{\circ}\text{C}$  until metabolomics analysis. Viable cell numbers in each sample were determined using trypan blue and used to normalize the metabolomics data. Prior to LC-MS analysis, samples were placed on ice and re-suspended with methanol:acetonitrile:water (5:3:2, v:v) at a concentration of  $2 \times 10^6$  cells/mL. Media samples were extracted with the same solution at a dilution of 1:25 (v/v). Suspensions were vortexed continuously for 30 min at  $4^{\circ}\text{C}$ . Insoluble material was removed by centrifugation at 18,000 g for 10 min at  $4^{\circ}\text{C}$  and supernatants were isolated for metabolomics analysis by UHPLC-MS.

Analyses were performed as previously published<sup>57, 58</sup>. Briefly, the analytical platform employs a Vanquish UHPLC system (ThermoFisher) coupled online to a Q Exactive mass spectrometer (ThermoFisher). Samples were resolved over a Kinetex C18 column,  $2.1 \times 150$  mm,  $1.7 \mu\text{m}$  particle size (Phenomenex, Torrance, CA) equipped with a guard column (SecurityGuard™ Ultracartridge – UHPLC C18 for 2.1 mm ID Columns – AJO-8782 – Phenomenex, Torrance, CA) using an aqueous phase (A) of water and 0.1% formic acid and a mobile phase (B) of acetonitrile and 0.1% formic acid for positive ion polarity mode, and an aqueous phase (A) of water:acetonitrile (95:5) with 1 mM ammonium acetate, and a mobile phase (B) of acetonitrile:water (95:5) with 1 mM ammonium acetate for negative ion polarity mode. Samples were eluted from the column using either an isocratic elution of 5% B flowed at  $250 \mu\text{L}/\text{min}$  and  $25^{\circ}\text{C}$  or a gradient from 5% to 95% B over 1 min, followed by an isocratic hold at 95% B for 2 min, flowed at  $400 \mu\text{L}/\text{min}$  and  $45^{\circ}\text{C}$ . The Q Exactive mass spectrometer (ThermoFisher) was operated independently in positive or negative ion mode, scanning in Full MS mode (2  $\mu\text{s}$  scans) from 60 to 900 m/z at 70,000 resolution, with 4 kV spray voltage, 45 sheath gas, 15 auxiliary gas. Calibration was performed prior to analysis using the Pierce™ Positive and Negative Ion Calibration Solutions (ThermoFisher). Acquired data was then converted from .raw to .mzXML file format using Mass Matrix (Cleveland, OH). Samples were analyzed in randomized order with a technical mixture injected periodically through analysis to qualify instrument performance. Metabolite assignments, isotopologue distributions, and correction for expected natural abundances of deuterium,  $^{13}\text{C}$ , and  $^{15}\text{N}$  isotopes were performed using

MAVEN (Princeton, NJ)<sup>59</sup>. Experiments were replicated twice (n=6 for drug treatment and n=4 for cell line phenotypes).

### 3D High-Content Screening.

High-content screening of 3D tumor organoids was conducted in the University of Colorado Anschutz Medical Campus, School of Pharmacy HTS core facility and NCATS. At the HTS core facility, the Janus Automation System (PerkinElmer) was used to plate and treat cells, while the Labcyte Echo Acoustic Liquid Handling system was used at NCATS. The HTS core utilized CellCarrier Spheroid ULA 96-well plates (PerkinElmer) and seeded the sorted M-phenotype SW620 cells at 5,000 cells/well in a volume of 75  $\mu$ L of growth medium. NCATS utilized Nexcelom3D ULA round bottom 384-well plates (Nexcelom, Lawrence, MA) and seeded at 2,000 cells/well in a volume of 40  $\mu$ L of growth medium. Afterwards, plates were centrifuged at 1,000 RPM for 10 min and a final concentration of 2% Matrigel was added to each well, with slow dispensing speed, to reach a final volume of 100  $\mu$ L/well and 50  $\mu$ L/well for the 96-well and 384-well format, respectively. Plates were then sealed with Breathable Film (Corning) and incubated at 37°C, 5% CO<sub>2</sub>, and 95% humidity control for 72h prior to drug treatment. The positive control (7) and library compounds were screened at 10  $\mu$ M for 72h. Tumor organoids were then stained with 25  $\mu$ M of Hoechst 33342 (ThermoFisher) and incubated for 1–2h at 37°C and 5% CO<sub>2</sub> prior to imaging.

Image acquisition and analysis was performed using the Opera Phenix HCS system (PerkinElmer). Images were acquired with a 5x air objective and using four channels (Brightfield, Hoechst 33342, RFP, GFP), with the same excitation and emission spectra as described above. A total of seven Z-slices were acquired each separated by 26.5  $\mu$ m, which were used to generate a maximum projection image for subsequent analysis using the Harmony 4.0 software (PerkinElmer) or Columbus Image Analysis System (PerkinElmer). Briefly, the spheroid was located by using the Brightfield and Hoechst 33342 channels. Then, the mean RFP and GFP intensity for the tumor organoid was calculated. The data was analyzed and normalized plate-wise to corresponding intra-plate neutral controls (0.1% DMSO). A Z'-factor was calculated for each screening plate using an RFP/GFP ratio. Mean and standard deviation values of normalized RFP and GFP intensities were calculated from each compound library. For hits that induce MET, we performed dose-response experiments twice (n=3)

## Supplementary Material

Refer to Web version on PubMed Central for supplementary material.

## Acknowledgements

This research was supported in part by grants awarded to D.V.L. from the Department of Defense Peer Reviewed Cancer Research Program (W81XWH-18-1-0142), the NIH NCI (1R01CA251361-01), and The ALSAM Foundation Therapeutic Innovation Grant. T.N. was supported by a NIH Training Grant (5T32HL7171-42). S.R. was supported by the Cancer Foundation of Luxembourg. We thank the Eli Lilly and Company Open Innovation Drug Discovery Program, particularly Evan Castetter and Maria Jose Lorite, for providing the BIC library. We also thank CU AMC shared resource laboratories, including the Drug Discovery and Development Shared Resource (HTS/HCS Discovery Arm), MS Metabolomics, Flow Cytometry, and NMR. These shared resources are supported in part by the UCCC NIH NCI designated cancer center (P30CA046934). We are grateful to Claudia Esquer for graphic design input of Fig. 6.

## References

1. Hanahan D, Weinberg RA. Hallmarks of cancer: the next generation. *Cell* 2011; 144: 646–674. [PubMed: 21376230]
2. Dongre A, Weinberg RA. New insights into the mechanisms of epithelial-mesenchymal transition and implications for cancer. *Nat Rev Mol Cell Biol* 2019; 20: 69–84. [PubMed: 30459476]
3. Voon DC, Huang RY, Jackson RA, Thiery JP. The EMT spectrum and therapeutic opportunities. *Mol Oncol* 2017; 11: 878–891. [PubMed: 28544151]
4. Chaffer CL, San Juan BP, Lim E, Weinberg RA. EMT, cell plasticity and metastasis. *Cancer Metast Rev* 2016; 35: 645–654.
5. Kroger C, Afeyan A, Mraz J, Eaton EN, Reinhardt F, Khodor YL et al. Acquisition of a hybrid E/M state is essential for tumorigenicity of basal breast cancer cells. *Proc Natl Acad Sci U S A* 2019; 116: 7353–7362. [PubMed: 30910979]
6. Yang J, Antin P, Berx G, Blanpain C, Brabletz T, Bronner M et al. Guidelines and definitions for research on epithelial-mesenchymal transition. *Nat Rev Mol Cell Biol* 2020; 21: 341–352. [PubMed: 32300252]
7. McDonald PC, Dedhar S. The role of epithelial-mesenchymal transition in cancer metastasis. In: Regad T, Sayers TJ, Rees RC(eds). *Principles of stem cell biology and cancer future applications and therapeutics*, 1st edn. John Wiley & Sons, Ltd: West Sussex, UK, 2015, pp 101–121.
8. Yun JA, Kim SH, Hong HK, Yun SH, Kim HC, Chun HK et al. Loss of E-Cadherin Expression Is Associated with a Poor Prognosis in Stage III Colorectal Cancer. *Oncology* 2014; 86: 318–328. [PubMed: 24924873]
9. Richardson F, Young GD, Sennello R, Wolf J, Argast GM, Mercado P et al. The evaluation of E-Cadherin and vimentin as biomarkers of clinical outcomes among patients with non-small cell lung cancer treated with erlotinib as second- or third-line therapy. *Anticancer Res* 2012; 32: 537–552. [PubMed: 22287743]
10. Dhanasekaran SM, Barrette TR, Ghosh D, Shah R, Varambally S, Kurachi K et al. Delineation of prognostic biomarkers in prostate cancer. *Nature* 2001; 412: 822–826. [PubMed: 11518967]
11. Kashiwagi S, Yashiro M, Takashima T, Nomura S, Noda S, Kawajiri H et al. Significance of E-cadherin expression in triple-negative breast cancer. *Br J Cancer* 2010; 103: 249–255. [PubMed: 20551954]
12. Ye Z, Zhang X, Luo Y, Li S, Huang L, Li Z et al. Prognostic Values of Vimentin Expression and Its Clinicopathological Significance in Non-Small Cell Lung Cancer: A Meta-Analysis of Observational Studies with 4118 Cases. *PLoS One* 2016; 11: e0163162. [PubMed: 27657690]
13. Toiyama Y, Yasuda H, Saigusa S, Tanaka K, Inoue Y, Goel A et al. Increased expression of Slug and Vimentin as novel predictive biomarkers for lymph node metastasis and poor prognosis in colorectal cancer. *Carcinogenesis* 2013; 34: 2548–2557. [PubMed: 24001454]
14. Rodriguez-Pinilla SM, Sarrío D, Honrado E, Moreno-Bueno G, Hardisson D, Calero F et al. Vimentin and laminin expression is associated with basal-like phenotype in both sporadic and BRCA1-associated breast carcinomas. *J Clin Pathol* 2006; 60: 1006–1012. [PubMed: 17105822]
15. Sciacovelli M, Frezza C. Metabolic reprogramming and epithelial-to-mesenchymal transition in cancer. *FEBS J* 2017; 284: 3132–3144. [PubMed: 28444969]
16. Tam WL, Weinberg RA. The epigenetics of epithelial-mesenchymal plasticity in cancer. *Nat Med* 2013; 19: 1438–1449. [PubMed: 24202396]
17. Zeisberg M, Neilson EG. Biomarkers for epithelial-mesenchymal transitions. *J Clin Invest* 2009; 119: 1429–1437. [PubMed: 19487819]
18. Brier B, Pierce SE, Kroeger C, Stover DG, Pattabiraman DR, Thiru P et al. Integrin-beta4 identifies cancer stem cell-enriched populations of partially mesenchymal carcinoma cells. *Proc Natl Acad Sci U S A* 2017; 114: E2337–E2346. [PubMed: 28270621]
19. Bighetti-Trevisan RL, Sousa LO, Castilho RM, Almeida LO. Cancer Stem Cells: Powerful Targets to Improve Current Anticancer Therapeutics. *Stem Cells Int* 2019: 1–15.
20. Yeung TM, Gandhi SC, Wilding JL, Muschel R, Bodmer WF. Cancer stem cells from colorectal cancer-derived cell lines. *Proc Natl Acad Sci U S A* 2010; 107: 3722–3727. [PubMed: 20133591]

21. Batlle E, Clevers H. Cancer stem cells revisited. *Nat Med* 2017; 23: 1124–1134. [PubMed: 28985214]
22. Mani SA, Guo W, Liao MJ, Eaton EN, Ayyanan A, Zhou AY et al. The epithelial-mesenchymal transition generates cells with properties of stem cells. *Cell* 2008; 133: 704–715. [PubMed: 18485877]
23. Esquer H, Zhou Q, Abraham AD, LaBarbera DV. Advanced High-Content-Screening Applications of Clonogenicity in Cancer. *SLAS Discov* 2020; 25: 734–743. [PubMed: 32484006]
24. Franken NA, Rodermond HM, Stap J, Haveman J, van Bree C. Clonogenic assay of cells in vitro. *Nat Protoc* 2006; 1: 2315–2319. [PubMed: 17406473]
25. Leggett SE, Sim JY, Rubins JE, Neronha ZJ, Williams EK, Wong IY. Morphological single cell profiling of the epithelial-mesenchymal transition. *Integrative biology : quantitative biosciences from nano to macro* 2016; 8: 1133–1144. [PubMed: 27722556]
26. Ackland ML, Newgreen DF, Fridman M, Waltham MC, Arvanitis A, Minichiello J et al. Epidermal growth factor-induced epithelial-mesenchymal transition in human breast carcinoma cells. *Lab Invest* 2003; 83: 435–448. [PubMed: 12649344]
27. Li Q, Chen C, Kapadia A, Zhou Q, Harper MK, Schaack J et al. 3D Models of epithelial-mesenchymal transition in breast cancer metastasis: high-throughput screening assay development, validation, and pilot screen. *J Biomol Screen* 2011; 16: 141–154. [PubMed: 21297102]
28. Abraham AD, Esquer H, Zhou Q, Tomlinson N, Hamill BD, Abbott JM et al. Drug Design Targeting T-Cell Factor-Driven Epithelial-Mesenchymal Transition as a Therapeutic Strategy for Colorectal Cancer. *J Med Chem* 2019; 62: 10182–10203. [PubMed: 31675229]
29. Zhou Q, Abraham AD, Li L, Babalморad A, Bagby S, Arcaroli JJ et al. Topoisomerase II $\alpha$  mediates TCF-dependent epithelial-mesenchymal transition in colon cancer. *Oncogene* 2016; 35: 4990–4999. [PubMed: 26947016]
30. Li H, Ning S, Ghandi M, Kryukov GV, Gopal S, Deik A et al. The landscape of cancer cell line metabolism. *Nat Med* 2019; 25: 850–860. [PubMed: 31068703]
31. Longo N, Frigeni M, Pasquali M. Carnitine transport and fatty acid oxidation. *Biochim Biophys Acta* 2016; 1863: 2422–2435. [PubMed: 26828774]
32. Hale JS, Otvos B, Sinyuk M, Alvarado AG, Hitomi M, Stoltz K et al. Cancer stem cell-specific scavenger receptor CD36 drives glioblastoma progression. *Stem Cells* 2014; 32: 1746–1758. [PubMed: 24737733]
33. Ye H, Adane B, Khan N, Sullivan T, Minhajuddin M, Gasparetto M et al. Leukemic Stem Cells Evade Chemotherapy by Metabolic Adaptation to an Adipose Tissue Niche. *Cell Stem Cell* 2016; 19: 23–37. [PubMed: 27374788]
34. Sánchez-Tilló E, de Barrios O, Siles L, Cuatrecasas M, Castells A, Postigo A.  $\beta$ -catenin/TCF4 complex induces the epithelial-to-mesenchymal transition (EMT)-activator ZEB1 to regulate tumor invasiveness. *Proc Natl Acad Sci USA* 2011; 108: 19204–19209. [PubMed: 22080605]
35. Marcucci F, Stassi G, De Maria R. Epithelial-mesenchymal transition: a new target in anticancer drug discovery. *Nat Rev Drug Discov* 2016; 15: 311–325. [PubMed: 26822829]
36. Zhang JH, Chung TDFAUO, Oldenburg KR. A simple statistical parameter for use in evaluation and validation of high throughput screening assays. *Journal of Biomolecular Screening* 1999: 67–73. [PubMed: 10838414]
37. Buchser W, Collins M, Garyantes T, Guha R, Haney S, Lemmon V et al. Assay Development Guidelines for Image-Based High Content Screening, High Content Analysis and High Content Imaging. In: Sittampalam GS, Gal-Edd N, Arkin M, Auld D, Austin C, Bejcek B et al (eds). *Assay Guidance Manual*: Bethesda (MD), 2004- [Updated 2014].
38. Jia D, Lu M, Jung KH, Park JH, Yu L, Onuchic JN et al. Elucidating cancer metabolic plasticity by coupling gene regulation with metabolic pathways. *Proc Natl Acad Sci U S A* 2019; 116: 3909–3918. [PubMed: 30733294]
39. San-Millan I, Julian CG, Matarazzo C, Martinez J, Brooks GA. Is Lactate an Oncometabolite? Evidence Supporting a Role for Lactate in the Regulation of Transcriptional Activity of Cancer-Related Genes in MCF7 Breast Cancer Cells. *Front Oncol* 2019; 9: 1536. [PubMed: 32010625]
40. Martinez-Outschoorn UE, Prisco M, Ertel A, Tsirigos A, Lin Z, Pavlides S et al. Ketones and lactate increase cancer cell “stemness,” driving recurrence, metastasis and poor clinical outcome

in breast cancer: achieving personalized medicine via Metabolo-Genomics. *Cell Cycle* 2011; 10: 1271–1286. [PubMed: 21512313]

41. Faubert B, Li KY, Cai L, Hensley CT, Kim J, Zacharias LG et al. Lactate Metabolism in Human Lung Tumors. *Cell* 2017; 171: 358–371 e359. [PubMed: 28985563]
42. Vlachostergios PJ, Oikonomou KG, Gibilaro E, Apergis G. Elevated lactic acid is a negative prognostic factor in metastatic lung cancer. *Cancer biomarkers : section A of Disease markers* 2015; 15: 725–734.
43. Walenta S, Chau TV, Schroeder T, Lehr HA, Kunz-Schughart LA, Fuerst A et al. Metabolic classification of human rectal adenocarcinomas: a novel guideline for clinical oncologists? *J Cancer Res Clin Oncol* 2003; 129: 321–326. [PubMed: 12827509]
44. Choi BJ, Park SA, Lee SY, Cha YN, Surh YJ. Hypoxia induces epithelial-mesenchymal transition in colorectal cancer cells through ubiquitin-specific protease 47-mediated stabilization of Snail: A potential role of Sox9. *Scientific reports* 2017; 7: 15918. [PubMed: 29162839]
45. Raimundo N, Baysal BE, Shadel GS. Revisiting the TCA cycle: signaling to tumor formation. *Trends Mol Med* 2011; 17: 641–649. [PubMed: 21764377]
46. Wise DR, DeBerardinis RJ, Mancuso A, Sayed N, Zhang XY, Pfeiffer HK et al. Myc regulates a transcriptional program that stimulates mitochondrial glutaminolysis and leads to glutamine addiction. *Proc Natl Acad Sci U S A* 2008; 105: 18782–18787. [PubMed: 19033189]
47. Serrano-Gomez SJ, Maziveyi M, Alahari SK. Regulation of epithelial-mesenchymal transition through epigenetic and post-translational modifications. *Molecular cancer* 2016; 15: 18. [PubMed: 26905733]
48. Cojoc M, Peitzsch C, Kurth I, Trautmann F, Kunz-Schughart LA, Telegeev GD et al. Aldehyde Dehydrogenase Is Regulated by beta-Catenin/TCF and Promotes Radioresistance in Prostate Cancer Progenitor Cells. *Cancer Res* 2015; 75: 1482–1494. [PubMed: 25670168]
49. Moore SF, van den Bosch MT, Hunter RW, Sakamoto K, Poole AW, Hers I. Dual regulation of glycogen synthase kinase 3 (GSK3)alpha/beta by protein kinase C (PKC)alpha and Akt promotes thrombin-mediated integrin alphaIIb beta3 activation and granule secretion in platelets. *J Biol Chem* 2013; 288: 3918–3928. [PubMed: 23239877]
50. Jacobsen A, Bosch LJW, Martens-de Kemp SR, Carvalho B, Sillars-Hardebol AH, Dobson RJ et al. Aurora kinase A (AURKA) interaction with Wnt and Ras-MAPK signalling pathways in colorectal cancer. *Scientific reports* 2018; 8: 7522. [PubMed: 29760449]
51. Lee SK, Hwang JH, Choi KY. Interaction of the Wnt/beta-catenin and RAS-ERK pathways involving co-stabilization of both beta-catenin and RAS plays important roles in the colorectal tumorigenesis. *Adv Biol Regul* 2018; 68: 46–54. [PubMed: 29449169]
52. Wang C, Shao L, Pan C, Ye J, Ding Z, Wu J et al. Elevated level of mitochondrial reactive oxygen species via fatty acid  $\beta$ -oxidation in cancer stem cells promotes cancer metastasis by inducing epithelial-mesenchymal transition. *Stem Cell Res Ther* 2019; 10: 175–175. [PubMed: 31196164]
53. Beharry Z, Mahajan S, Zemskova M, Lin YW, Tholanikunnel BG, Xia Z et al. The Pim protein kinases regulate energy metabolism and cell growth. *Proc Natl Acad Sci U S A* 2011; 108: 528–533. [PubMed: 21187426]
54. Bai F, Asojo OA, Cirillo P, Ciustea M, Ledizet M, Aristoff PA et al. A novel allosteric inhibitor of macrophage migration inhibitory factor (MIF). *J Biol Chem* 2012; 287: 30653–30663. [PubMed: 22782901]
55. Zhang X, Chen L, Wang Y, Ding Y, Peng Z, Duan L et al. Macrophage migration inhibitory factor promotes proliferation and neuronal differentiation of neural stem/precursor cells through Wnt/beta-catenin signal pathway. *Int J Biol Sci* 2013; 9: 1108–1120. [PubMed: 24339732]
56. Zhang FX, Ge SN, Dong YL, Shi J, Feng YP, Li Y et al. Vesicular glutamate transporter isoforms: The essential players in the somatosensory systems. *Prog Neurobiol* 2018; 171: 72–89. [PubMed: 30273635]
57. Nemkov T, Hansen KC, D'Alessandro A. A three-minute method for high-throughput quantitative metabolomics and quantitative tracing experiments of central carbon and nitrogen pathways. *Rapid Commun Mass Spectrom* 2017; 31: 663–673. [PubMed: 28195377]

58. Nemkov T, Reisz JA, Gehrke S, Hansen KC, D'Alessandro A. High-Throughput Metabolomics: Isocratic and Gradient Mass Spectrometry-Based Methods. *Methods Mol Biol* 2019; 1978: 13–26. [PubMed: 31119654]
59. Clasquin MF, Melamud E, Rabinowitz JD. LC-MS data processing with MAVEN: a metabolomic analysis and visualization engine. *Curr Protoc Bioinformatics* 2012; Chapter 14: Unit14 11.

Author Manuscript

Author Manuscript

Author Manuscript

Author Manuscript

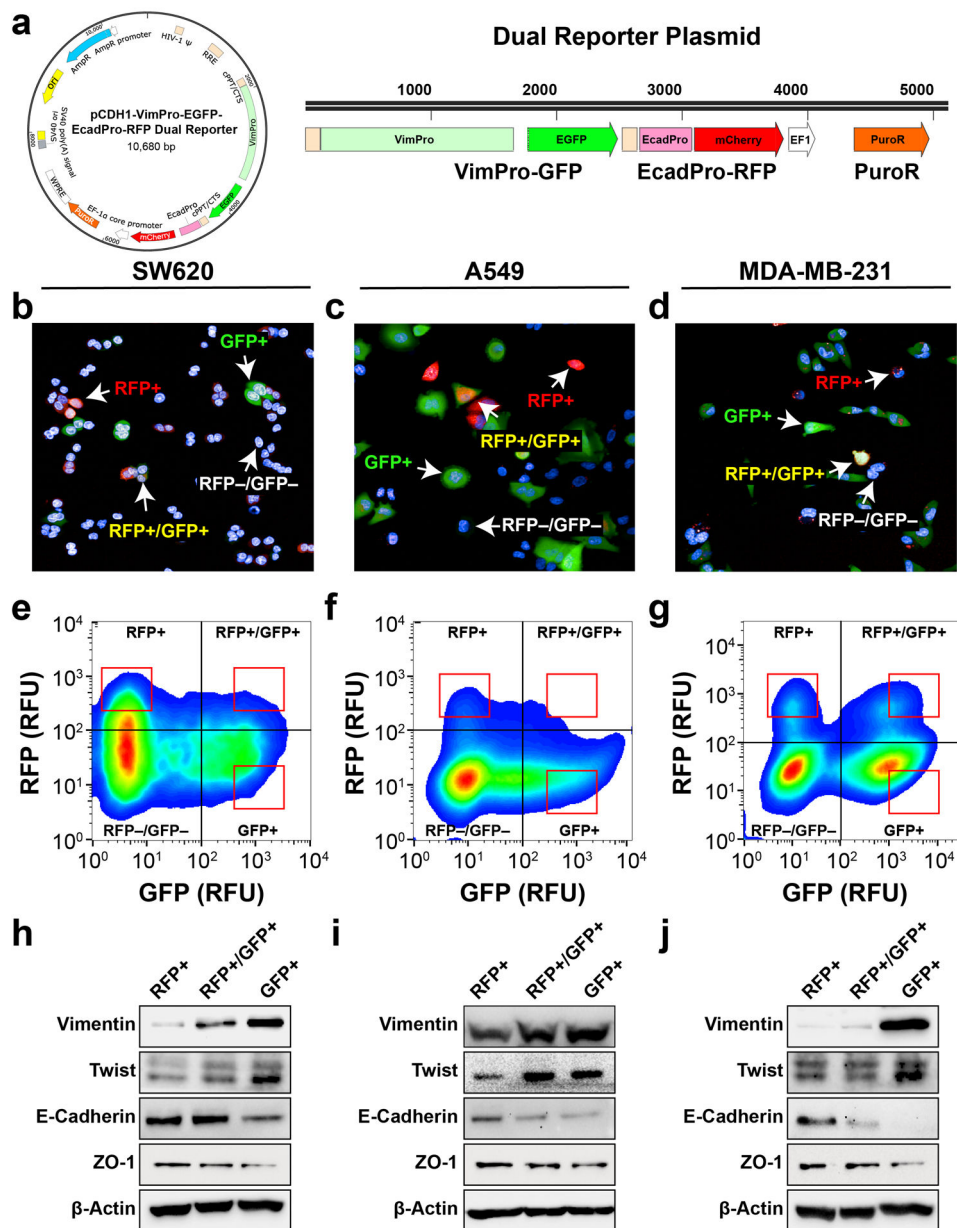


**Fig. 1. The dual-reporter allows for the identification and isolation of distinct EMT subtypes.** (a) Fluorescent dual-reporter plasmid map, VimPro-GFP (vimentin promoter reporter); EcadPro-RFP (E-cadherin promoter reporter). (b-d) Confocal images of SW620, A549, and MDA-MB-231 dual-reporter unsorted cell lines (20x water objective). Fluorescent channels: Blue (Hoechst 33342), Green (GFP), Red (RFP). (e-g) FACS distribution of the dual-reporter cell lines. (h-j) Representative western blots of sorted phenotypes using known EMT markers. Mesenchymal markers: vimentin and Twist. Epithelial markers: E-cadherin and ZO-1.

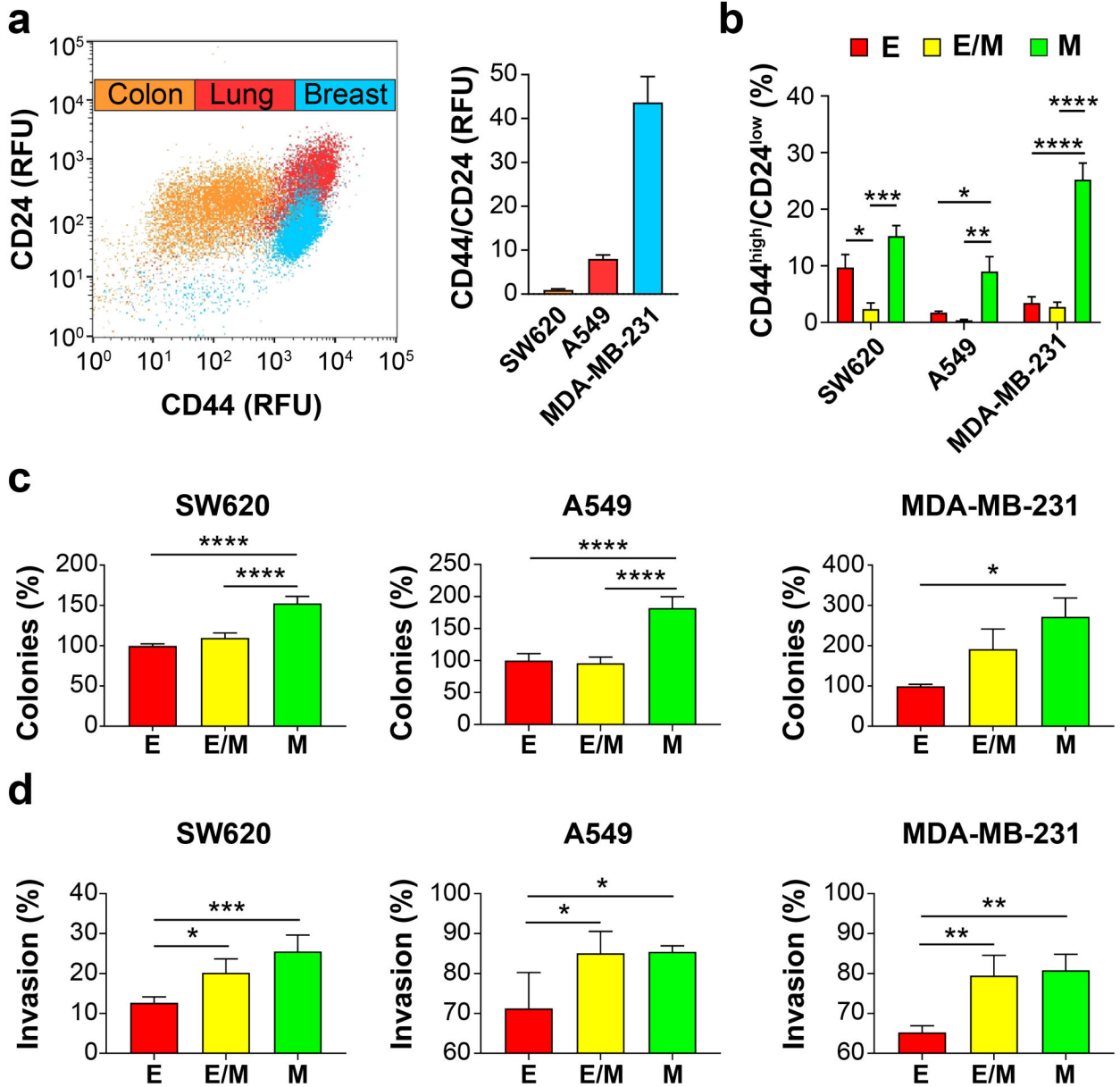


**Fig. 2. The mesenchymal phenotype has higher stemness and invasive potential.**

(a) Gated flow cytometry distribution of SW620, A549, and MDA-MB-231 cells by the immunofluorescent staining of CD44 and CD24 and quantification of the CD44/CD24 ratio of the different cell lines. (b) Unsorted cells gated for CD44<sup>high</sup>/CD24<sup>low</sup> were further categorized to each EMT phenotype based on their dual-reporter fluorescence (mean ± SEM). *P*-values were generated by two-way ANOVA. (c) Quantification of the stemness within the EMT phenotypes for the various cell lines. Data is normalized to the E-phenotype (mean ± SEM). *P*-values were calculated by one-way ANOVA. (d) Tumor cell invasion assay quantification of the different cell lines. Graphs show the ability of the tumor cells to close a scratch wound while embedded in Matrigel. Mean ± SD of a singlet experiment from quadruplicate wells. *P*-values were calculated by one-way ANOVA.

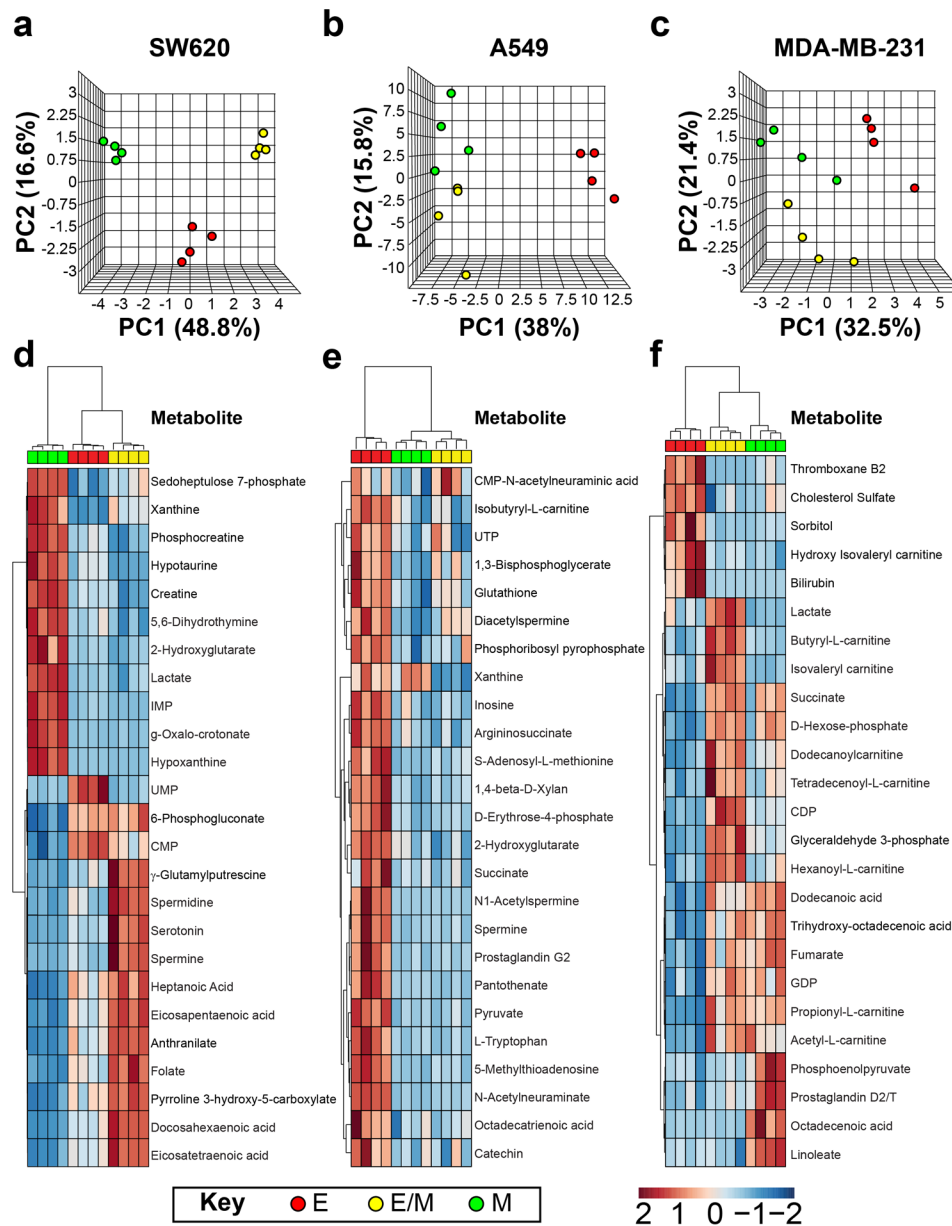


**Fig. 3. Isolated EMT cell populations have distinct metabolotypes.**

Isolated EMT phenotypes were assessed for metabolotypes using LC-MS-based metabolomics. (a,b,c) Steady-state metabolomics reveals distinct metabolotypes by PCA. (d,e,f) Hierarchical Clustering Analysis graphed as heat maps with metabolites (4 replicates). The differences between the EMT phenotypes were exclusively described by PC1 and PC2, while PC3 described technical variability: SW620 (9.8%), A549 (10.2%), and MDA-MB-231 (12.6%). Each column of each heat map refers to an individual sample, with the same color code as the PCA as indicated in the figure key. Metabolite levels are plotted according to relative abundance using a color gradient from red to blue for highest to lowest level, respectively.

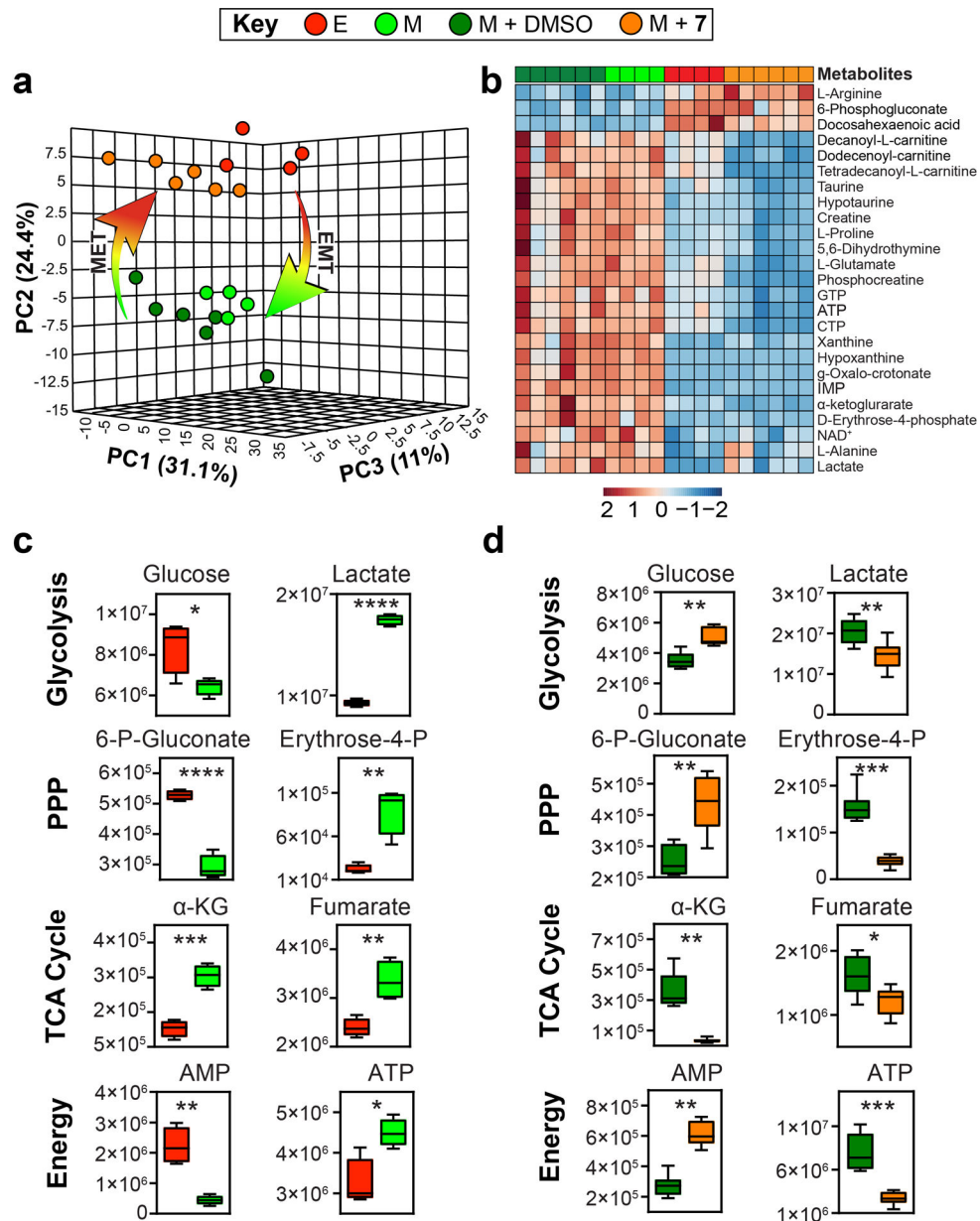


**Fig. 4. Treatment of M-phenotype CRC tumor organoids with 7 induces MET by metabolomics.** (a) PCA of SW620 tumor organoids comprised of E or M cells (4 replicates), and M cells treated with DMSO or 7 (6 replicates). To control for inherent batch variability stemming from independent dataset acquisition, metabolites in each sample were normalized to the median value in the respective M sample group. The metabolic differences shared between E and M+7 organoids relative to M are described by PC2. (b) The 25 metabolites with the largest magnitude of loading weights along PC2 were hierarchically clustered and graphed as a heat map. Metabolite levels are plotted according to relative abundance using a color gradient from red to blue for highest to lowest level, respectively. Each column refers to an individual sample, with the same color code as the PCA as indicated in the figure key. (c) Box-whisker plots are shown for the E and M levels of metabolites involved in

glycolysis, pentose phosphate pathway (PPP), tricarboxylic acid (TCA) cycle, and energy status. (d) Box-whisker plots are shown for these same metabolites in M-phenotype cells treated with DMSO or **7**, Y-axis values represent raw unnormalized peak areas in arbitrary units. *P*-values were calculated using the Student's t-test.

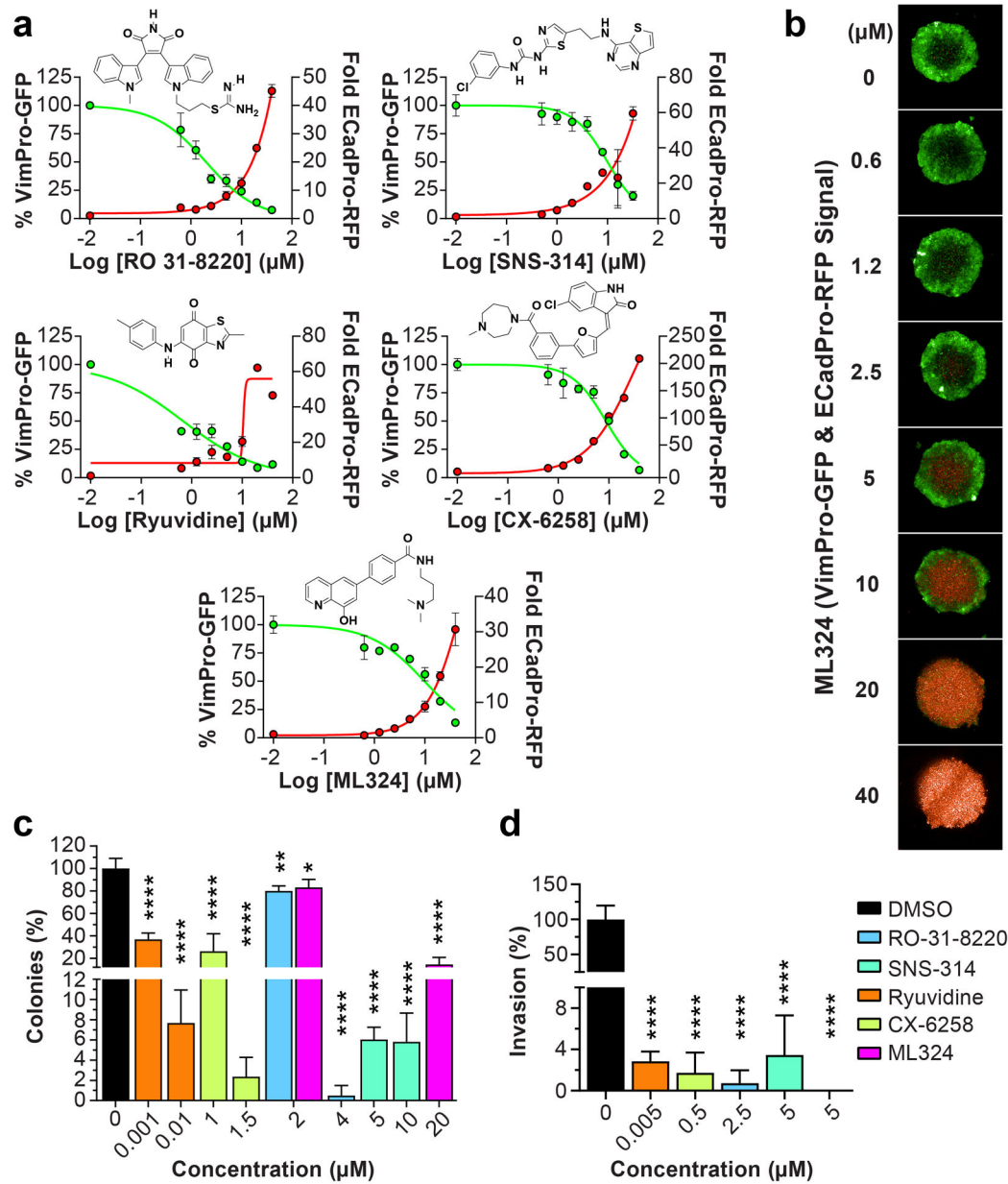


**Fig. 5. A diverse set of probes reverse EMT in a dose-dependent manner.**  
 (a) Dose-response graphs of lead EMT probes that induce MET (mean  $\pm$  SD). (b) Representative fluorescent images (10x air objective) of tumor organoids treated with ML324. (c) Quantification of the stemness in SW620 M-phenotype cells treated with lead probes. Data is normalized to DMSO control (mean  $\pm$  SD). *P*-values were calculated by two-way ANOVA. (d) Tumor cell invasion of SW620 cells treated with lead probes. Data is normalized to DMSO control. Mean  $\pm$  SD of a singlet experiment from quadruplicate wells. *P*-values were calculated by one-way ANOVA.

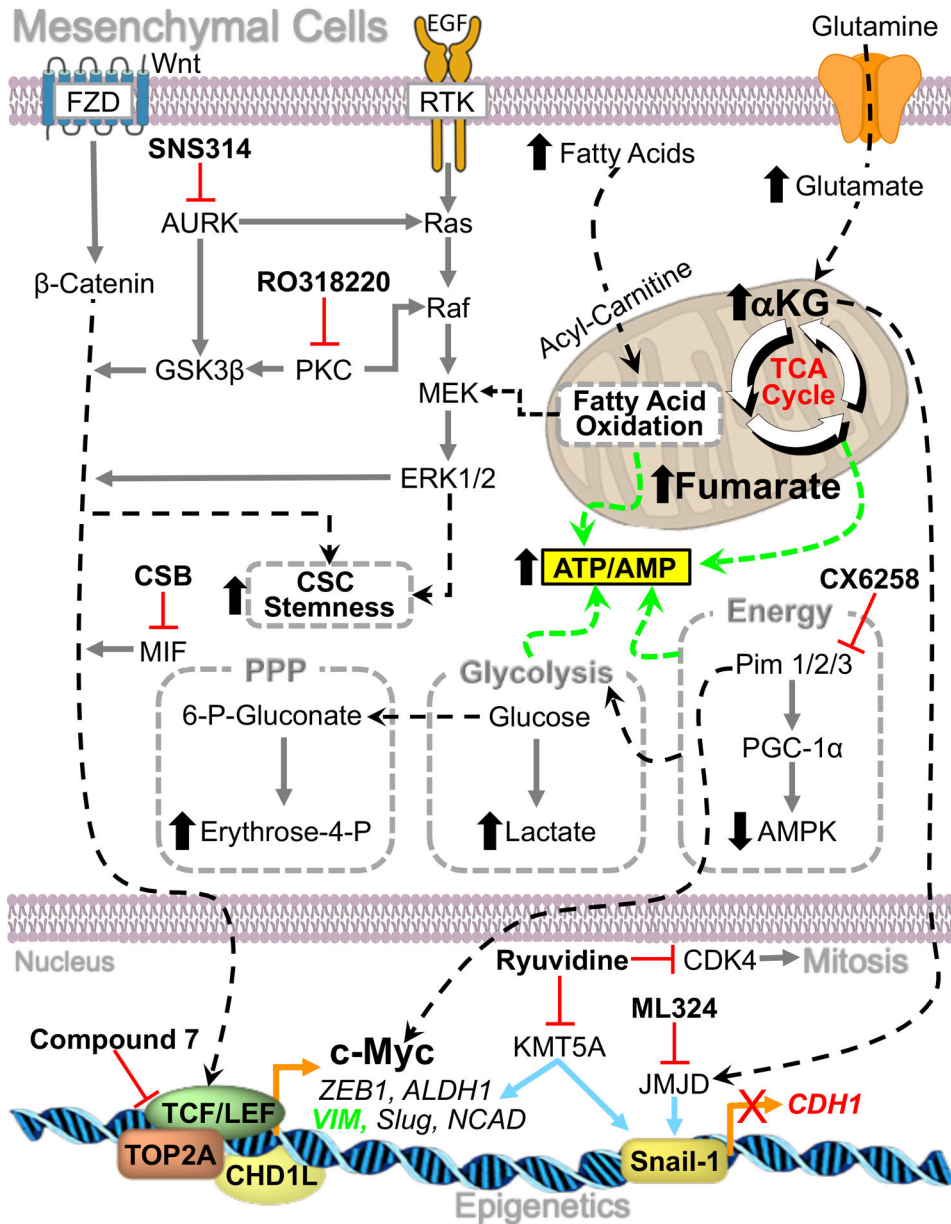


**Fig. 6. Mechanisms regulating mesenchymal cell EMP in CRC.** EMP is orchestrated by a series of cellular processes (black dashed arrows), including signal transduction (grey arrows), bioenergetics (green dashed arrows), epigenetic events (light blue arrows), and transcription factors (orange arrows). The processes regulating mesenchymal cell EMP have been elucidated using isolated SW620 M-phenotypes. Lead probes capable of inducing MET (red blunt headed arrow indicating target inhibition) and the results from the metabolomics studies were used to infer a coherent relationship between probe molecular targets and processes regulating mesenchymal cell plasticity in CRC.